Innovative sample preparation and handling strategies for automated and high-throughput metabolomics

Miggiels, A.L.W.

Citation

Miggiels, A. L. W. (2024, March 12). *Innovative sample preparation and handling strategies for automated and high-throughput metabolomics*. Retrieved from https://hdl.handle.net/1887/3721725

Chapter 5

Automated online preconcentration of biomass-limited samples into a sub-microliter droplet using machine-vision-controlled evaporation

Paul Miggiels, Yupeng He, Bert Wouters, Leander Boer, Cees van der Geld, Amy Harms, Isabelle Kohler, Thomas Hankemeier

Manuscript in preparation

Abstract

As the field of bioanalysis matures, there is a growing need for high-throughput and highly sensitive analysis of biomass-limited samples. Common sample preparation methods are often challenged in their ability for automation and handling of small-volume or highly-diluted samples, which compromises the full potential of state-of-the-art separation and detection techniques. In this study, we present a strategy to address this issue with the development of fully automated, on-line sample preconcentration by solvent evaporation from a pendant droplet into a (sub-)microliter volume. A droplet of 500 nL is formed at the distal end of a syringe needle, placed in a flow of nitrogen at elevated temperature. The droplet is kept at constant volume using machine-vision feedback to adjust the nitrogen flow, while sample solution is continuously injected into the droplet via the syringe. This setup was built into a robotic autosampler to fully automate the process. Evaporation rates of 6 µL/min were achieved from a droplet of 500 nL volume, which consisted of 50-80% methanol or acetonitrile in water. The evaporation parameters were optimized with the aid of a theoretical model. A 15-fold preconcentration was obtained in less than 3 min, visualized using a methylene blue dye. With the direct integration into an autosampler, our setup can be readily integrated into existing bioanalytical workflows. This was demonstrated by the 10-fold preconcentration of amino acids and direct coupling to liquid chromatograph – mass spectrometry analysis, which resulted in an approximately 10-fold increase in peak height. This proof of concept on a selected set of analytes highlights the potential impact and versatility of our approach for analysis of biomass-limited samples in a large diversity of bioanalytical fields where a high sensitivity and/or throughput are crucial, including metabolomics.

Introduction

In the last decade, metabolomics, i.e., the comprehensive analysis of all – or as many as possible relevant – metabolites in an organism, has become an important pillar among the -omics approaches in clinical and drug research[1–5]. Indeed, gaining deeper insights into metabolic pathways can contribute to a better understanding of disease mechanisms, as well as the discovery of novel biomarkers candidates and potential drug targets[1,6]. Among the pool of metabolites, present in an organism (>215,000 compounds reported in the recent Human Metabolome Database 5.0[7]), a large number is present at trace levels, requiring state-of-the-art high-sensitive analytical approaches for their analysis. In addition, it is common that such low-abundant metabolites need to be identified and quantified in biomass-limited samples[8,9], which can be diluted by nature (e.g., dialysates), concentrated but low in volume (e.g., animal tissue samples, biopsies, organoids or selected cell fractions), or both diluted and low in volume (e.g., microdialysates[10,11] and organ-on-a-chip perfusates[12]). Lastly, the large number of samples, including quality control samples, that typically need to be measured in large-scale metabolomics cohorts underlines the need for faster analysis methods and automation of the entire metabolomics workflow for round-the-clock operation[13–15].

Liquid chromatography – mass spectrometry (LC-MS) is considered the gold standard analytical approach in metabolomics, due to its high sensitivity, selectivity and reasonable throughput[15,16]. Over the last years, mass spectrometers have seen tremendous improvements to enable the detection of trace metabolite levels in complex matrices. Similarly, numerous improvements have been carried out to improve the chromatographic performance and extend the metabolome coverage, such as the use of sub-2-µm fully porous particles, sub-3-µm superficially porous particles, alternative modes such as hydrophilic interaction chromatography (HILIC), or the use of supercritical fluid chromatography[14,16–19]. However, less efforts have been put in the development of innovative high-throughput, automated sample preparation approaches enabling the preconcentration of low-abundant metabolites in biomass-limited samples. Moreover, despite the use of state-of-the-art chromatographic approaches in metabolomics, often a significant gap remains between the ideal sample composition required to reach the highest chromatographic performance and the actual sample composition after sample preparation. This is especially true for more complex chromatographic approaches, such as HILIC[20] and miniaturized approaches, such as micro-, capillary-, and nano-LC[21], where the separation efficiency is largely influenced by the injected volume and injection solvent. When analyzing analytes of a large polarity range, a balance has to be found between a good solvent and still a not too good eluent when injecting a reasonable sample volume onto the separation column. Thus, in general, chromatographic separations benefit from injecting low-volume but high-concentration samples, among other reasons to ease the influence of the solvent.

The complexity of biological samples often requires the use of selective extractions prior to the injection, typically liquid-liquid extraction (LLE) or solid-phase extraction (SPE). Subsequently, the extraction solvent is evaporated and reconstituted in an adequate injection solvent. However, this workflow is less suitable for low-volume samples and offers limited preconcentration potential for dilute samples. Miniaturized approaches, or microextractions, are designed to work with low sample volumes and achieve high concentration factors[22–26], but still have significant challenges to overcome regarding automation and scalability for high-throughput workflows[27–29].

Alternatively, electrokinetic sample preparation approaches are promising in providing simultaneous extraction and enrichment, but are aimed only at charged analytes[30–34]. Fornells et al. presented a non-selective, inline preconcentration device by partial solvent evaporation through a semipermeable membrane, but this approach is time-consuming (60 min. for 30-fold preconcentration) and designed for continuous flow applications rather than discrete samples[35]. So far, a dedicated approach is lacking that can keep up with increasingly fast separations (a few minutes or faster), and can easily be automated and hyphenated to various analysis platforms.

In this study, we present an online and fully automated method for evaporative sample preconcentration, that is integrated in a commercial robotic autosampler. Solvent is evaporated from a suspended droplet using vision-controlled feedback to concentrate the analytes. The concentrated droplet can then be directly coupled to standard LC-MS equipment. In a previous pilot study, we presented a proof-of-concept for solvent switching using machine-vision controlled evaporation from a hanging droplet for offline liquid chromatography – nuclear magnetic resonance (LC-NMR) modulation[36]. This setup, however, was limited in automation because of the syringe pump used, and transferred the samples by reconstituting the droplet in a different solvent.

In the current study, the setup was further developed, characterized and optimized, and implemented in an automated workflow. A theoretical model was built and compared with experimental observations to derive essential parameters and predict the performance limits of the evaporative process. The preconcentration effect was demonstrated by 10-fold preconcentration of methylene blue dye with an evaporation rate of 6 μL/min. Furthermore, the evaporation parameters, namely, droplet size, gas temperature and solvent composition were investigated and optimized. Finally, the potential of this method for metabolomics applications was demonstrated by fully automated, online preconcentration of amino acids and direct coupling to reversed-phase LC-MS analysis. In addition, the hanging droplet evaporator was further characterized for the analysis of esters using gas chromatography with flame ionization detection. The obtained results show the future possibilities of incorporating of this setup into any bioanalytical workflow, enabling for high-throughput and high-sensitive analysis of biomass-limited samples for metabolomics.

Materials and methods

Chemicals and samples

Methanol (MeOH) of LC-MS grade was purchased from Actu-All (Oss, The Netherlands). MilliQ water was obtained using a Millipore high-purity water dispenser (Sigma-Aldrich, Zwijndrecht, The Netherlands). Methylene blue dye, L-tryptophane and L-valine were purchased from Sigma-Aldrich, and L-isoleucine was purchased from Cambridge Isotope Laboratories Inc. (Tewksbury, MA, USA).

Samples of methylene blue were prepared from a stock solution of 1 mg/mL methylene blue in water, and diluted to the desired concentration with 50% MeOH in water. A mix of amino acid standards was prepared from a stock solution with analyte concentrations of 50 μg/mL in 50% MeOH, and further diluted in 50% MeOH to 3.125 ng/mL for analysis.

For samples analysed with gas chromatography, esters mix including dimethyl phthalate (DMP), diethyl phthalate (DEP), di-n-butyl phthalate (DBP) and benzyl butyl phthalate (BBP) were purchased from Sigma-Aldrich, and methanol was obtained from Biosolve (Valkenswaard, The Netherlands). The same water system as aforementioned was used. Samples were prepared with a concentration of 20 μg/mL for each ester, in either 90% MeOH in water.

Evaporation module and operation

Figure 1A illustrates the principle of the hanging droplet evaporator principle. The concept is similar to the preliminary set-up developed by Schoonen et al.[36]. A droplet is formed at the distal end of a needle and is exposed to a flow of heated nitrogen gas. While fresh sample is continuously dispensed into the droplet, the solvent is evaporated from the droplet surface at an equal rate to maintain a constant droplet volume. The droplet volume is continuously measured by a camera and real-time image processing. A feedback control loop maintains the droplet at constant volume by adjusting the nitrogen flow accordingly. After a set volume of sample is dispensed and evaporated, and thereby the preconcentration factor reached, the process is stopped and the droplet is used for further analysis.

The process takes place in a CTC PAL3 RTC autosampler (CTC Analytics AG, Zwingen, Switzerland) (Figure 1B). The autosampler holds a 25 μL glass syringe with a removable, flat-point, 1.3 mm outer and 0.2 mm inner diameter stainless steel needle (Setonic GmbH, Ilmenau, Germany). The integration with the autosampler works as follows. The autosampler aspirates the initial sample volume, including a potential rear air gap, moves to the droplet evaporation module and lowers the needle into the droplet evaporation module. The sample is dispensed at a constant rate so that a droplet is formed at the tip of the needle. While the sample is dispensed, the droplet volume is monitored real-time with a camera system. This value serves as input for a feedback loop that regulates the flow of hot nitrogen flow into the system, so that the influx of sample into the droplet is in equilibrium with the evaporative outflux at the droplet surface. This effectively ensures that the droplet remains at constant volume while the solvent evaporates and analytes are concentrated in the droplet. After the evaporation the remaining preconcentrated sample is drawn up in the syringe again and can be used for further processing or analysis. The effective concentration factor can be calculated as:

$$CF = \frac{V_{initial}}{V_{final}}. \tag{1}$$

The heart of the evaporation module is the evaporation chamber (Figure 1C). This part is entirely machined out of poly-ethylene ether ketone (PEEK) for its thermal and chemical resistance. Two PEEK bodies mated together form the horizontal flow channel for the gas flow. Halfway this channel, there is a vertical entry point for the syringe needle. Moreover, two optical windows are embedded in the channel wall at this position to provide optical access, namely, a clear window for the camera and an opaque window to diffuse the backlight. The flow channel starts as circular cross section at the in- and outlet, and gradually and symmetrically tapers to a non-circular shape at the optical windows to minimize disturbances to the airflow. The droplet is imaged at 10 frames per second with a Basler Pulse puA1600-60uc colour CMOS camera (Basler AG, Ahrensburg, Germany), fitted with a 2x zoom telecentric lens (TechSpec® CompactTL™ 2x magnification, 40 mm working distance, Edmund Optics Ltd., York, United Kingdom). The fixed magnification of the lens ensures a fixed pixel size of 2.25x2.25 μm.

The nitrogen flow is firstly regulated with a Bronkhorst EL-Flow mass flow controller (Bronkhorst, The Netherlands) and subsequently heated with a 500 W hot-air soldering heating element (Eleshop BV, Eindhoven, The Netherlands) in a custom enclosure, that is positioned directly at the inlet of the evaporation chamber. The inlet portion of the evaporation module is equipped with a needle preheater, consisting of a aluminium rod with 1.4 mm diameter centre through-hole for the needle and a 10W Kapton® flexible heating element on the outside (Omega Engineering

Limited, Manchester, United Kingdom). The module is fitted with four thermocouples: an integrated J-type inside the gas heater element, and three K-type thermocouples at the chamber inlet and outlet, and the needle preheater (0.15x150 mm, Omega Engineering Limited, Manchester, United Kingdom) and an 8-channel thermocouple interface (ADAM 4118, Advantech Co., Ltd., Taipei, Taiwan).

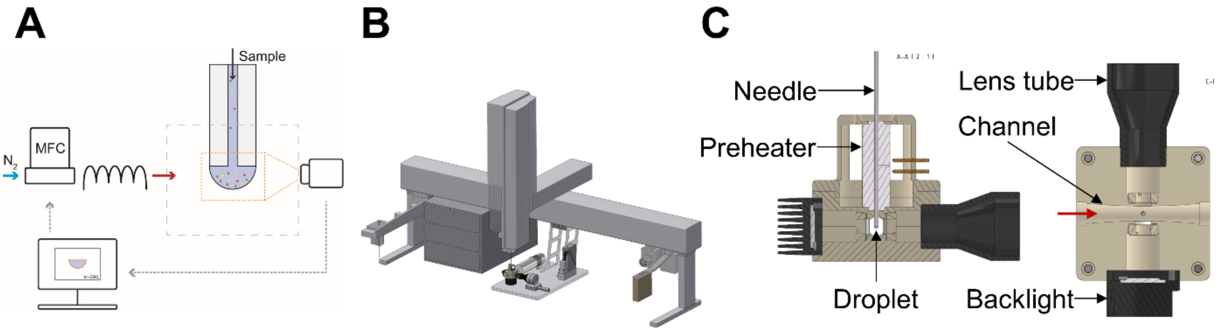

Figure 1. Schematic overview of the automated droplet evaporation preconcentration module. A) Schematic representation of the evaporative preconcentration principle; B) CTC PAL3 robotic autosampler with integrated droplet evaporation module; C) Detailed cross-sections of the evaporation chamber showing the channel cross-section at the droplet (left) and the lofted profile of the gas flow channel (right).

Automation

The CTC PAL3 autosampler is programmed and controlled via PAL Sample Control 2.50. The droplet evaporation module was programmed in the autosampler as general Injector-module with adjustable penetration depth. This depth was calibrated once so that the droplet was in the center of the camera view. The evaporation module and process are controlled with a custom LabView application, using the Vision Development and Control & Simulation packages (LabView 2020 SP1, National Instruments, Austin, Texas, USA). The LabView application and PAL Sample Control share sample details via a common text file, and synchronize their activities using contact closures. Upon the needle entering the evaporation module, PSC writes sample information such as name, droplet volume and temperature setpoints, to the shared text file and sends a contact closure to the LabView application. The application, in turn, reads the sample parameters, waits for the temperatures to reach their setpoint, and stores a binary image of the needle without droplet. After this initialization procedure, a contact closure is sent to the autosampler to start dispensing the sample and the LabView application starts the process of controlled evaporation. When the autosampler has finished dispensing the set sample volume, the droplet is retracted and a trigger signal is sent to the LabView application to end the process. The droplet volume is calculated real-time with a custom algorithm (step-by-step images in Supplementary Information S1). Firstly, the image is binarized based on a set threshold and connected holes within the droplet and needle perimeter are filled. Next, the binary image of the needle, as stored during sample initialization, is subtracted to obtain a binary matrix of the droplet profile. The droplet volume can then be calculated using disc integration along the vertical axis, using the sum of each row as the diameter of the disc, as presented in Eq. 2, in which d_{px} is the known dimension of a square pixel, equal to 2.25 μm. Since the gas flow is perpendicular to the line of sight, it is assumed that the droplet only deforms in the visual plane; therefore, each disc is axisymmetric. With this assumption, the droplet profile as a whole does not have to be axisymmetric.

$$V_{droplet} = \frac{\pi}{4} d_{px}^3 \sum_{i=1}^{n} \sum_{j=1}^{n} x_{i,j}^2 \tag{2}$$

The droplet volume is used as reference for the proportional-integral (PI) controller in the LabView application to regulate the nitrogen gas flow between 0.4 and 8 L/min, thereby adjusting the evaporation rate. Temperature of the nitrogen gas flow and preheater are maintained constant with an in-house programmed Arduino Mega 2560 (Arduino, Italy) and the Arduino PID library v1.1, and custom electronics to modulate the heaters. The Arduino collects the temperature readouts the thermocouple interface via RS-485 and passes these to the LabView application via serial communication. Simultaneously, the PID controller modulates the heater power using the pulse-width modulation (PWM) outputs of the Arduino. These PWM output pins are set to operate at 31 kHz. The preheater power is modulated with a simple optocoupler switching circuit. For the nitrogen heater a special circuitry was designed to operate at the high PWM frequency and thereby minimize feedback of high-frequency noise from the high switching load back into mains.

Experimental evaporation rate

The experimental mass transfer rate of water drops, at various ambient conditions, was determined by forming a 2.5 μL droplet inside the evaporation module and letting it evaporate under static conditions in the evaporation chamber. The temperature and mass flow of the gas were set and equilibrated before the measurement. The evaporation rate $\frac{\delta V}{\delta t}$ was then calculated from the resulting volume-time profile at a the interval $V = 500 \pm 50$ nL.

Sample preconcentration

All samples were preconcentrated at a rate of 6 μL/min using a droplet volume setpoint of 500 nL, preheater temperature of 50 °C, nitrogen gas temperature of 230 °C, and maximum gas flow rate of 8 L/min. Methylene blue samples were concentrated from 12 to 0.8 μL (CF=15), amino acid standard samples were preconcentrated from 8 to 0.8 μL (CF=10). For the partial loop injection, the sample was bracketed by air gaps of 2 μL at the rear and 3 μL at the front, respectively, and injected at a flow rate of 6 μL/min.

Liquid chromatography – mass spectrometry

The LC-MS analysis was performed using a Waters Acquity UPLC system hyphenated via electrospray ionization (ESI) to a Waters Xevo TQ-MS Triple Quadrupole mass spectrometer (Waters, Milford, MA, USA). The separation was performed using a Kinetex C18 column (2.1 × 50 mm, 1.7 μm, Phenomenex, Torrance, CA, USA). The mobile phase was composed of water with 0.1% formic acid (solvent A) and MeOH with 0.1% formic acid (solvent B). The separation was carried out using the following gradient: start with 0% B; 35% B at 1.5 min.; 90% B at 1.6 min; maintain 90% B until 3.0 min.; 0% B at 3.1 min.; maintain 0% B until 5.0 min. The ESI source was operating in positive mode, with the following parameters: ESI voltage, 3 kV; temperature, 150 °C; cone voltage, 30 V; cone gas flow rate 50 L/h; desolvation gas flow rate, 1000 L/h; and collision gas flow rate, 0.10 mL/min. MS data was acquired using timed multi reaction monitoring mode (MRM), with the following timings and transitions (window, precursor > fragment, collision energy): leucine, 0.35-0.56 min, 132.17 > 86.17 m/z, 10 eV; tryptophane, 0.7-3.5 min, 205.23 > 118.29 m/z, 30 eV; valine, 0.1-0.38 min, 118.15 > 72.15 m/z, 10 eV.

Characterization with gas chromatography – flame ionization detection (GC-FID)

For the characterization of esters using GC-FID, the autosampler was fitted with a 25 μL glass syringe, having a fixed, 22s gauge needle. Evaporation was performed with a droplet volume of 500 nL, preheater temperature of 50 °C, gas temperature of 80 °C, maximum gas flow rate of 6 L/min.

The samples were concentrated to a final volume of 1 μL, and the initial volumes were 1, 2, 4, 6, 8, 10, 12, 15, 20, and 22 μL, which corresponds to expected concentration factors of 1-22.

GC-FID analysis of the esters was performed on a Thermo Fischer TRACE 1310 with 23 gauge Merlin seal and flame ionization detector. The injection method was splitless with surge, with the following parameters: split flow: 6.0 mL/min; splitless time: 0.5 min; purge flow: 5.0 mL/min; temperature: 280 °C; surge pressure: 200 kPa; surge duration: 0.5 min. An Agilent J&W HP-5MS UI column with 30 m length, 0.25 mm diameter and 0.25 μm film was used to separate the esters. The separation method was as follows: 0-2 min: 50 °C; 2-7 min: 50-210 °C; 7-17.3 min: 210-280 °C; 18 min: stop. The detector was set to 280 °C and a hydrogen flow of 45 mL/min.

Results and discussion

Optimization of the automated evaporation

The droplet evaporation module was successfully integrated in the robotic autosampler (Figure 1B). In this configuration, the system was capable of consecutively preconcentrating series of samples in a fully automated fashion, whereby all sample parameters could be programmed for each individual sample. For optimal throughput, the software maintained the last-used gas temperature for up to 300 s in between samples to minimize the equilibration time for consecutive samples. In practice, this is ideal when the temperature difference between consecutive samples is minimal, which is often the case when processing batches of samples.

Tuning the PI controller parameters is essential to maintaining a stable droplet volume throughout the process. After careful tuning, the droplet volume stayed within ±50 nL of the setpoint volume of 500 nL (Supplementary Information S2). The evaporative process is an integrating process, meaning that at a given output of the actuator (i.e., the gas flow), the process value (i.e., the droplet volume) does not reach an equilibrium value. Therefore, the controller gains could not be tuned with classical methods for self-regulating systems, such as Ziegler-Nichols or Cohen-Coon, and the lambda tuning rules were used[37,38]. The initial gains were determined by measuring the process dead time from a step test in open loop mode and fine-tuned by hand, resulting in optimized proportional gain $K_p = 16.0$, integration time $T_i = 1.5$ s and derivative time $T_d = 0.0$ s.

Modelling of aqueous droplet evaporation

The evaporation from drops is a long-studied phenomena; Ranz & Marshall studied already in 1952 the evaporation of drops in a free stream and described the heat and mass transfer analogy to approximate this mechanism[39]. Here, their initial work was adapted to a hemispherical droplet in a free stream. An imaginary fin was added to represent the needle as a solid rod with a diameter equal to the droplet base diameter (Figure 2A). Since the flow is normal to the axis of the droplet and the cylinder, a boundary layer develops along the droplet surface and, as such, strong local differences exist, i.e., the mass transfer will be higher upstream than downstream[40]. As a reasonable approximation, a solution to the coupled heat and mass balance is here obtained using well-established empirical correlations that are valid for these conditions, and are in terms of averaged gas concentration and temperature. For the droplet in the free stream, the correlation by Ranz & Marshall was used[39], and the Hilpert correlation was used for the needle as cylinder in a cross flow[41]. Furthermore, the following assumptions were made for the model: the process is in steady state; all physical properties are constant; the temperature is uniform over the droplet surface; the physical properties can be evaluated at the film temperature, which is the arithmetic mean of the free stream temperature (T_∞) and the droplet surface temperature (T_d); the effect of radiative heat transfer is negligible; nitrogen gas leaves the mass flow controller at 293 K; and the needle is a cylindrical rod with a finite length of 3 mm.

Ultimately, these conditions lead to a coupled heat and mass balance according to Equation 3, with $\dot{m}$ the mass transfer rate; ΔH_{LV} the latent heat of evaporation; h_d and h_n the convective heat transfer coefficients of the droplet and needle, respectively; R the droplet radius, equal to the needle radius; L the needle length; T_∞ and T_d the temperature of the free stream and the droplet surface, respectively; and η_{fin} the fin efficiency. The solution for this non-linear problem can be found by iteratively solving for T_d, the droplet surface temperature. The full set of equations and material properties are described in Supplementary Information S3.

$$\dot{m}\Delta H_{LV} = h_d 2\pi R^2 (T_\infty - T_d) + h_n 2\pi R L (T_\infty - T_d)\eta_{fin} \tag{3}$$

Comparison between model prediction and experimental data

The predicted and measured evaporation rates, illustrated in Figure 2B, exhibit a similar trend, namely, *i)* the mass transfer increases with increasing free stream temperature and velocity, and *ii)* the evaporation rate is in the range of 1-5 µL/min ($1.8\text{-}7.22\cdot10^{-8}$ kg/s). The model predictions deviate up to 30% from the experimental values and overall provide a good approximation of the evaporation rate in this setup. Although the model supports an increase in evaporation rate with increasing free stream temperature and velocity, practical limits to these parameters were observed. Firstly, free stream temperatures above 160 °C may induce vapor bubble nucleation inside the droplet at the contact area with the needle, as the needle rapidly heats up in the crossflow. These vapor bubbles result in instability of the droplet as they grow and/or disrupt the interface (Supplementary Information S4). Secondly, at free stream velocities above 7 m/s, the droplet surface deformation becomes too large, which can hinder accurate determination of the droplet volume, and can even lead to the contact line breaking and the droplet adhering to the outer surface of the needle.

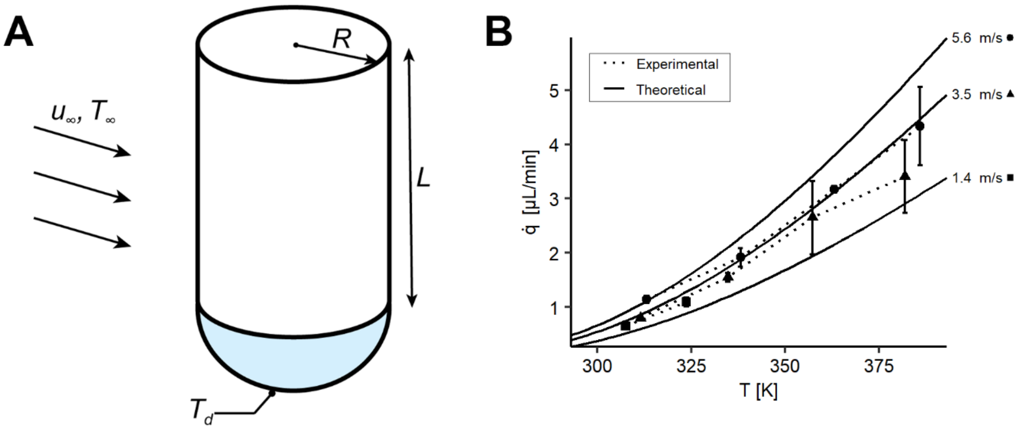

Figure 2. A) Schematic of the hemispherical droplet on a cylindrical rod; B) Theoretical and experimental evaporation rates of a hemispherical water droplet with a base radius of 1.3 mm at free stream velocities of 1.4-5.6 m/s and temperatures of 300-393 K.

Model considerations

Obviously, the proposed model approximates reality and is simplified with reasonable assumptions to maintain a solvable set of equations. Most notably, mass transfer is determined with empirical correlations for a free, spherical droplet and a free cylinder in a crossflow. To the best of our knowledge, specific correlations for a hemispherical droplet on a cylindrical rod have not been reported yet. When computing mass transfer from a correlation for a spherical geometry (with the appropriate contact area), the presence of a contact line, where the local mass transfer is inherently higher, is not taken into account. Alternatively, Ganzevles & Geld provide a correlation for a hemispherical droplet on a plate, which includes a contact line. Their correlation only differs from Ranz & Marshall in the values of the coefficients, but not significantly.[42] The coefficients for a hemispherical droplet on a rod would be between that of the free spherical droplet and the hemispherical droplet on a plate. Therefore, it can be reasonably assumed that either correlation will provide a sufficiently accurate approximation for a hemispherical droplet. If the geometry changes from hemispherical to a truncated sphere, the correlation of Ganzevles & Geld is more appropriate.

Another limitation of the model is that these surface-averaged properties do not take into account the deformation of the droplet surface by the crossflow. This oscillating deformation, as shown in Figure 3, positively contributes to the mass transfer. In order to include this parameter, a correlation for oscillating surfaces would need to be found that not only relates to surface-averages, but also to time-averages. Alternatively, the model could be improved by empirically determining the average transfer coefficients for a hemispherical droplet on a cylindrical rod. However, the complexity of this endeavor is beyond the scope of the present work.

Lastly, the model assumes a solid cylinder of 3 mm length as the needle, because this is the part exposed to the free stream. In reality, the needle is a 55-mm hollow tube and liquid sample at ambient temperature is dispensed through the needle into the droplet. In addition, the remaining needle length that is covered by the needle heater at the chamber entry can provide additional heat flux to the droplet if the heater is enabled ($T > T_{amb}$) or may act as a heatsink otherwise. All these phenomena are not considered in the present model and may account for the differences found in Fig. 2B.

Sample preconcentration by evaporation

Based on the model predictions, evaporation rates of 4-5 µL/min are to be expected for aqueous drops. However, the robotic autosampler has a minimum dispensing rate of 6 µL/min. In order for the droplet evaporation process to work, the rate of evaporation from the droplet surface has to match the constant influx of sample as dispensed by the autosampler. In many analytical applications, the solvent is composed of a mixture of water and organic solvent. Most commonly-used organic solvents in LC, such as methanol and acetonitrile, have a higher vapour pressure than water and therefore increase the evaporation rate. Thus, the addition of volatile organic solvents to the sample solvent can aid in achieving the required evaporation rate of 6 µL/min.

The effect of automated analyte preconcentration by solvent evaporation from a hanging droplet was demonstrated with preconcentrating methylene blue dye in a solution of 50% MeOH in water from a droplet volume of 500 nL and a liquid dispensing rate of 6 µL/min. Methylene blue is an ionic and non-volatile molecule; therefore, it is ideally suited for visualization purposes. Figure 3 shows a selection of captured frames of the process, highlighting the increase of the dye concentration in the droplet over time as the sample is continuously fed into the droplet while the solvent is evaporated from the droplet surface at an equal rate.

This method of preconcentrating analytes is ideally suited for thermolabile metabolites, many of which have shown to degrade at temperatures above 100 °C[43]. Due to evaporative cooling from the droplet surface, the surface temperature remains below the wet-bulb temperature, i.e. the temperature of the gas saturated with vapor, which is much lower than the boiling point[39,44,45]. According to the model predictions the surface temperature of the droplet does not exceed 60 °C under the circumstances used here, which should have little influence on metabolites according to Fang et al.[43].

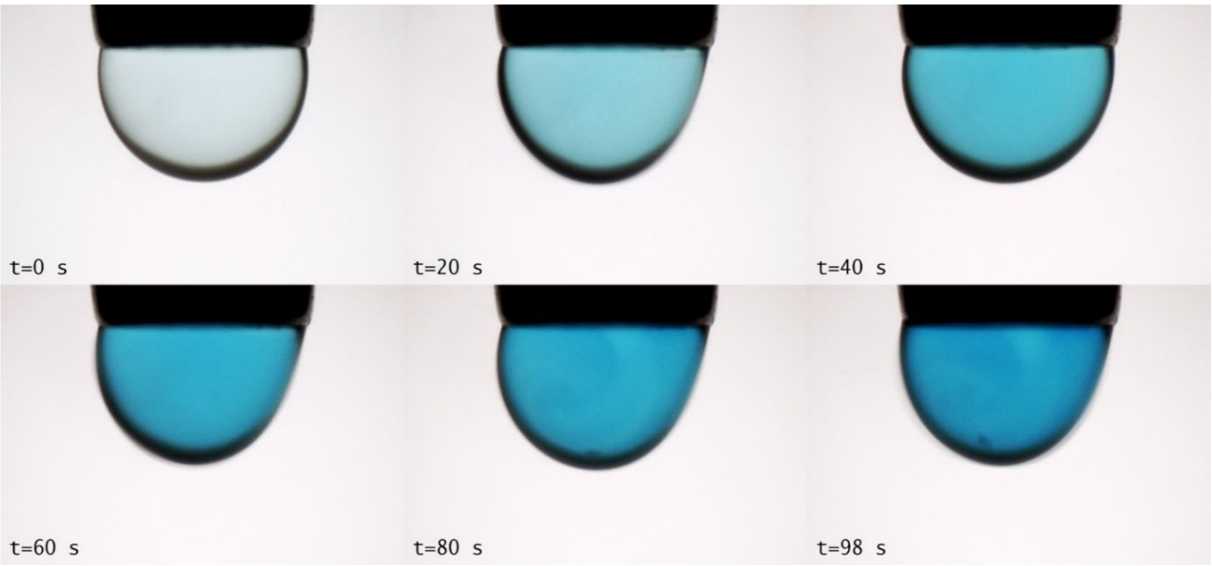

Figure 3. Fifteen-fold preconcentration (from 12 to 0.8 μL) of methylene blue in water:MeOH 1:1 (v:v) solution with an initial concentration of 5 μg/mL in ca. 3 min.

It is worth mentioning that the presence of non-volatile solutes, such as salts and enzymes – which are typically expected in biological samples – can cause an elevation of the boiling point[46]. The concentration of methylene blue used here is low enough not to cause any noteworthy influence. For biological applications however, the samples would require sample preparation, for example dilution, protein precipitation, or a selective extraction, prior to the evaporation step to the extent that analytes that interfere with, or can precipitate during the evaporation process are sufficiently removed. In any application where large differences in analyte concentrations remain even after initial sample preparation, care should be taken not to preconcentrate any of the target analytes above their solubility limit and cause precipitation of the analyte, or above the saturation limit of the detection method, as this will disturb the metabolites ratio for biological interpretation of the data. The camera system would also allow to detect precipitation by means of particle detection algorithm that can be added, and the software could signal this event, if there is a reasonable risk of precipitation of analytes. The risk of exceeding the detector saturation limits has to be assessed for each specific bioanalytical application.

The work of Schoonen et al. demonstrated that there is little differentiation of the analytes based on their volatility; even volatile organic acids were recovered with about 100% recovery after the evaporation process[36]. However, this effect should also be carefully assessed for each application, as this differentiation can also alter the metabolite ratio and hence the biological interpretation.

Optimization of the evaporation parameters.

In order to maximize the evaporation rate from the droplet surface, four parameters can be adjusted according to Eq. 3, namely: *i)* higher free stream temperature, *ii)* higher free stream velocity *iii)* larger droplet surface (πR^2), and *iv)* lower the enthalpy of evaporation, for example by adding volatile organic solvent. As aforementioned, for aqueous drops the free stream temperature should be below 160 °C to prevent vapor bubble formation. Furthermore, the free stream velocity is limited to 7 m/s to maintain a stable droplet surface.

Trying to enlarge the droplet surface area creates a cascade of complications. To enlarge the surface of the hemispherical droplet, the droplet base radius, which is determined by the needle radius, has to be increased. The current 1.3 mm diameter needle is the maximum diameter that is compatible with standard modules in the autosampler ecosystem, such as the needle washing station and injection valves. Alternatively, the hemispherical droplet geometry can be abandoned for a truncated sphere of larger volume. Yet, the surface of this droplet geometry is prone to breaking from the gas flow, causing the sample to adhere to the needle outer surface and flow upwards on the needle. Additionally, increasing the droplet volume decreases the achievable concentration factor with the current 25 μL syringe (Eq. 1). This can be compensated for with a larger capacity syringe, but this in turn compromises the accuracy of handling low-microliter volumes that is necessary for the evaporation process and the transfer of the droplet thereafter.

Finally, by adding volatile organic solvent to the sample solution, the enthalpy of evaporation is reduced and the mass transfer is increased. At the same time, this increases the solubility of less polar analytes. In the example of methylene blue, the addition of methanol in the sample solution increased the evaporation rate of the solution above the minimum dispensing rate of the autosampler. However, the addition of volatile organic solvent also leads to a trade-off. The higher vapor pressure restricts the maximum free stream temperature, to prevent vapor bubble formation. Moreover, the surface tension decreases by adding organic solvent, which impairs the surface stability and therefore limits the maximum gas velocity[48,49]. Furthermore, in the case of a water:MeOH mixture, the final sample diluent becomes more aqueous, as methanol evaporates faster than water. Though this effect is expected to be limited because of the continuous influx of sample solution into the droplet, it should be carefully considered when dealing with less polar analytes close to the solubility limit. Several organic solvents, such as acetonitrile, ethanol, 2-propanol and n-butanol, can form an azeotrope in a binary mixture with water, i.e., a mixture with a constant boiling point whose composition remains unchanged when evaporated[50]. These binary azeotropes, however, typically occur at percentages of organic solvent at which the droplet stability for the evaporation process is compromised. Ternary azeotropes are unsuitable in this application, as these mostly occur at even lower fraction thereof.

The trade-off between the evaporation rate and analyte solubility on one hand and the stability of the droplet surface during evaporation on the other hand, is specific for each solvent mixture. For example, acetonitrile and water form an azeotrope at 80% acetonitrile. In experiments with mixtures of 50, 70, 80 and 90% acetonitrile, the solution with 50% acetonitrile was found not volatile enough to achieve the minimum evaporation rate of 6 μL/min. At 70 and 80% acetonitrile, the solution was sufficiently volatile, but at 80% acetonitrile the solution was prone to vapor bubble formation and the droplet surface breaking. Finally, at 90% acetonitrile, above the azeotropic point, the process was regularly disturbed by vapor bubble formation and the surface was unstable due to the reduced surface tension. These findings demonstrate that there is an optimum range for the fraction of organic for a given solvent, and this range needs to be determined experimentally for each application and matrix composition.

Integrated LC-MS analysis

A proof-of-concept of the preconcentration procedure with online coupling to LC-MS was demonstrated. A standard mixture of three amino acids was preconcentrated from an initial volume of 8 μL to a volume of 0.8 μL and directly injected in the LC-MS equipment, and compared to a control of 0.8 μL of the original standard mixture. The extracted ion chromatograms (Figure 4) show a drastic increase of 8- to 13-fold in peak height for the three amino acids after preconcentration, which supports the effect of analyte preconcentration from the hanging droplet. Where valine and tryptophane were hardly above the detection limit in the control sample, a clear peak is observed after preconcentration.

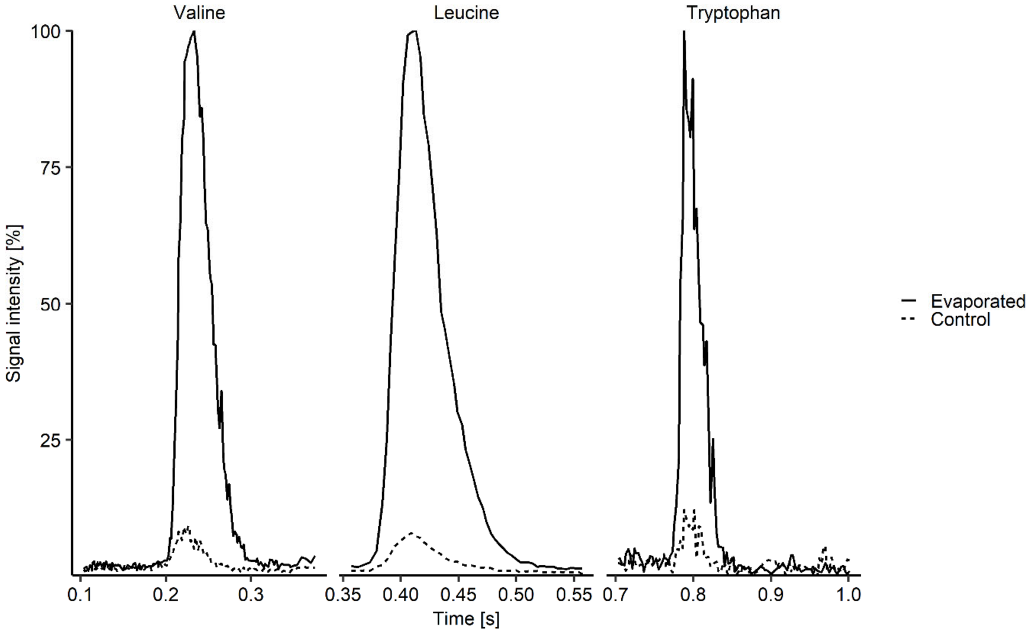

Figure 4. Extracted ion chromatograms of valine, leucine and tryptophane in control samples (dotted line) and after evaporation from 8 to 0.8 µL (solid line).

These results indicate that the droplet evaporation method allows for the concentrations of samples by controlled solvent evaporation. This step is important for chromatographic applications, as it is often beneficial to samples in lower volume but higher concentration[51,52]. In reverse-phase chromatography, the early eluting analytes especially benefit from injecting a smaller but more concentrated samples. Relatively polar analytes, such as amino acids, have little retention on reverse-phase columns and do not benefit from on-column focusing as less polar analytes do, and are therefore prone to peak broadening or peak shape distortion[53]. When injecting the same analyte mass but in a smaller volume, the diluent mixes more easily with the mobile phase and the peak shape of the polar analytes is improved. The same principle holds for HILIC, where the sample diluent is even more critical for the quality of the chromatography. Ruta et al. demonstrated that in a typical HILIC application using 95% acetonitrile as mobile phase, the peak shape rapidly deteriorates above 10% water in the sample diluent[20]. As aforementioned, a percentage of 90% acetonitrile would be too high for the droplet evaporation method. However, Ruta et al. also showed that good peak shape can still be achieved with lower percentage acetonitrile in the diluent if the injection volume is below 1% of the column volume[20].

The benefit of preconcentration prior to injection becomes perhaps even more so apparent in miniaturized chromatography. As miniaturized columns are susceptible to column overloading, the tolerable injection volumes are low, typically in the order of low-µL for micro-LC and low-nL for nano-LC, respectively[21,54–56]. By preconcentrating the sample into a suitable sub-microliter volume, more analyte mass can be injected to optimally profit from the separation efficiency and sensitivity of miniaturized separations – keeping in mind of course the limits for mass overloading.

Droplet injection to LC-MS

These examples demonstrate the sweet spot for the hanging droplet evaporation method, i.e., reducing the sample to a highly-concentrated, sub-microliter volume, which can be directly coupled to LC-MS. This can improve the chromatographic quality and ease the restrictions on the sample diluent, aiding the interfacing between sample preparation and subsequent chromatography. Nevertheless, transferring the droplet to the analytical system remains challenging, as the entire preconcentrated sample should be injected on the column to maximize the preconcentration potential, and this process should be repeatable. The autosampler is capable of two commonly used modes of injection with a switching valve, namely, full loop and partial loop injection. While full loop injection offers the best repeatability, the required loop overfill means a (large) part of the sample is still discarded[57–59]. Partial loop injection allows to position the entire sample inside the loop by using a loop volume several times that of the sample volume and bracketing the sample between air bubbles. When the sample is dispensed from the syringe into the sample loop, the sample plug elongates due to the inherent parabolic flow profile[52,60]. Therefore, as a rule of thumb, the injected volume should be no more than 50% of the loop volume to ensure acceptable repeatability, i.e., lower than 5%[54,60].

Here, we employed partial loop injections to be able to maintain the full droplet volume after sample reconcentration. Preliminary results of the injection repeatability, whereby 0.8 μL of amino acid standards was loaded in a conventional 5 μL stainless steel loop, showed a relative standard deviation (RSD) of the peak area of >10% (data not included). This is significantly higher than 1-2% RSD that is achievable in similar setups[61,62], and therefore impedes further characterization of the droplet evaporation process.

The high RSD of injection can be attributed to the combination of small injection volume and the loop used, with an inner diameter of 25 μm (0.001”). Partial loop injections are sensitive to accurate and precise positioning of the sample in the loop. With small volumes and small inner diameter loops, the effect of the parabolic flow profile is more pronounced and this is amplified by any variation in cross section along the length of the loop[60,63]. A possible solution for this would be to replace the drawn stainless steel loop with a loop specialized for small-volume injections, such as fused-silica that has better defined and more constant cross section. Once the injection repeatability is brought down to an acceptable level, the performance of the droplet evaporation method, in combination with subsequent analysis, can be further quantified.

Characterization by GC-FID

Finally, the droplet evaporation method was coupled to GC-FID as alternate injection technique and to further quantify the evaporative preconcentration process. The signal response correlates with the initial volumes with good linearity for all of the esters (Figure 5). Most importantly, the increase in peak area reflects the relative increase in initial volume (and thereby concentration factor). In other words, increasing the initial volume by a given factor resulted an equal increase in peak area. For example, when comparing 2 and 10 µL initial volume (CF=2 and CF=10, respectively), the peak area increased by a factor of 5. Similarly, when comparing 10 and 20 µL initial volume (CF=10 and CF=20, respectively), the peak area increased by a factor of 2. This indicates that the hanging droplet evaporator indeed achieves linear concentration of the analytes, with the expected concentration factor.

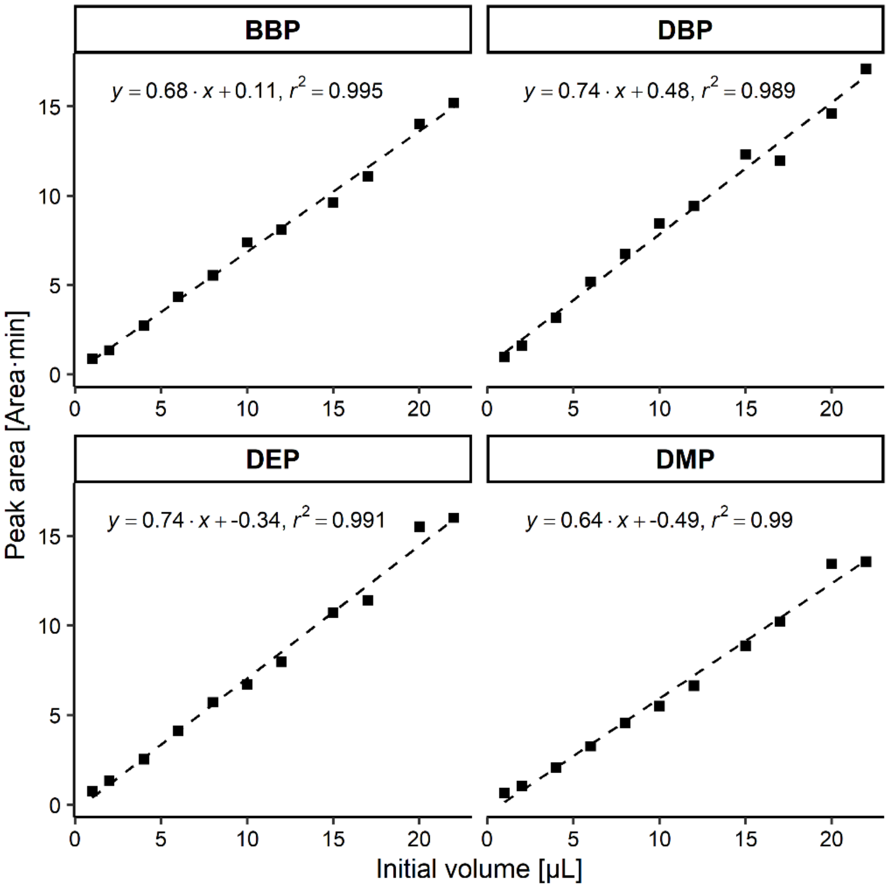

Figure 5. Peak area response of esters measured on GC-FID after droplet evaporation preconcentration into 1 µL from various starting volumes. The response shows good linearity to the concentration factor.

The repeatability of the process was evaluated at low, medium and high concentration factors for all analytes and showed good RSD of below 20% (Table 1). The RSD is highest at the low concentration factor, which can most likely be attributed to the low initial and final volumes, and the small ratio between the two. At these low volumes and ratio, small deviations in the initial or final volume, that can occur in aspirating the sample and in the evaporation process, respectively, propagate more strongly in the concentration factor and therefore the repeatability. This is supported by the declining trend in the RSD with increased initial volume for all analytes. Only DBP deviates from this trend, for which a probable cause can be found in its lower solubility compared to the other analytes.

In all, the RSDs could be improved by employing an internal standard, which was not done here. This will especially benefit the repeatability at low concentration factors.

In all, these GC-FID results demonstrate the capability of the droplet evaporation preconcentration technique. At the same time, it exemplifies the necessity of a good transfer method in order to exploit its full potential.

Table 1. Relative standard deviation (RSD) of esters DMP, DEP, DBP and BBP at concentration factor of 2, 10 and 20.

Concentration Factor	**RSD**			
	DMP	**DEP**	**DBP**	**BBP**
2	13.2%	9.5%	11.2%	18.1%
10	6.6%	9.0%	4.9%	6.3%
20	4.6%	2.4%	16.8%	3.6%

Conclusion

In this work, we present a method for fully automated sample preconcentration into a (sub-)microliter droplet, directly coupled to a state-of-the-art LC-MS setup. The preconcentration is performed by controlled evaporation of the sample solvent from a hanging droplet, that is maintained at a constant volume of 500 nL using machine-vision feedback to match the evaporation rate with the sample inflow rate. Using a theoretical model of the droplet evaporation, performance limits were predicted. The model showed good correspondence with experimental data, and aided in optimization of the evaporation parameters. With mixtures of 50-80% methanol or acetonitrile in water, stable droplet evaporation at a rate of 6 μL/min was achieved. At higher percentage of organic solvent the droplet interface became unstable with loss of the sample as result due to the decrease in surface tension of the sample. The principle of preconcentration into a droplet was then visualized by 15-fold preconcentrating, from 12 to 0.8 µL, of methylene blue dye in under 3 min. A clear increase in dye concentration was visible while the droplet volume remained around the preset volume throughout the process. LC-MS coupling was demonstrated as proof-of-concept by directly injecting a droplet of 10-fold preconcentrated sample of a set of amino acids, showing a significant increase in peak intensity for the preconcentrated sample. Finally, the performance of the hanging droplet evaporator was characterized for 1- to 22-fold preconcentration of a mixture of esters, which resulted in a linear and equal increase of the signal, with RSDs below 20%.

The current setup thus is capable of delivering highly concentrated, sub-microliter samples. With the correct transfer method to LC-MS injection, it can aid in sample solvent matching, peak broadening for early eluting compounds, or volume loading in (complex) chromatography applications. The transfer set-up for LC injection is currently further developed. The coupling to GC-FID showcases the versatility of this technique. This setup, being fully automated in a device-agnostic autosampler, can be readily integrated into existing metabolomics-based methods for the analysis of biomass-limited samples.

Acknowledgments

The authors are grateful for the help and support of Raphael Zwier (Fine Mechanical Department) and Harry Visser (Electronics Department) from Leiden University in designing and building the hanging droplet evaporator module. The authors also acknowledge the help of Tom Vercammen and colleagues from Interscience BV with the CTC PAL autosamplers. This work received funding from: the European Research Council (ERC) under the European Union's Horizon 2020 research and innovation programme under grant agreement No 667375; the European Funds for Regional Development (Kansen voor West II: Phenomix Fieldlab); and the Dutch Research Council (NWO) Investment Grant Large programme, as part of the Exposome-Scan project (project number 175.2019.032).

References

1. Beger, R. D. *et al.* Metabolomics enables precision medicine: "A White Paper, Community Perspective". *Metabolomics* **12**, 149 (2016).

2. Wörheide, M. A., Krumsiek, J., Kastenmüller, G. & Arnold, M. Multi-omics integration in biomedical research – A metabolomics-centric review. *Anal. Chim. Acta* **1141**, 144–162 (2021).

3. Pang, H., Jia, W. & Hu, Z. Emerging Applications of Metabolomics in Clinical Pharmacology. *Clin. Pharmacol. Ther.* **106**, 544–556 (2019).

4. Rinschen, M. M., Ivanisevic, J., Giera, M. & Siuzdak, G. Identification of bioactive metabolites using activity metabolomics. *Nat. Rev. Mol. Cell Biol.* **20**, 353–367 (2019).

5. Johnson, C. H. & Gonzalez, F. J. Challenges and opportunities of metabolomics. *J. Cell. Physiol.* **227**, 2975–2981 (2012).

6. Wishart, D. S. Emerging applications of metabolomics in drug discovery and precision medicine. *Nat. Rev. Drug Discov.* **15**, 473–484 (2016).

7. Wishart, D. S. *et al.* HMDB 5.0: The Human Metabolome Database for 2022. *Nucleic Acids Res.* **50**, D622–D631 (2022).

8. van Mever, M. *et al.* Mass spectrometry based metabolomics of volume-restricted in-vivo brain samples: Actual status and the way forward. *TrAC - Trends Anal. Chem.* **143**, 116365 (2021).

9. He, B. *et al.* Analytical techniques for biomass-restricted metabolomics: An overview of the state-of-the-art. *Microchem. J.* **171**, 106794 (2021).

10. Verbeeck, R. K. Blood microdialysis in pharmacokinetic and drug metabolism studies. *Adv. Drug Deliv. Rev.* **45**, 217–228 (2000).

11. Custers, M. L. *et al.* Applicability of cerebral open flow microperfusion and microdialysis to quantify a brain-penetrating nanobody in mice. *Anal. Chim. Acta* **1178**, 338803 (2021).

12. Junaid, A. *et al.* Metabolic response of blood vessels to TNFα. *Elife* **9**, 1–28 (2020).

13. Sumner, L. W. *et al.* Proposed minimum reporting standards for chemical analysis: Chemical Analysis Working Group (CAWG) Metabolomics Standards Initiative (MSI). *Metabolomics* **3**, 211–221 (2007).

14. Zampieri, M., Sekar, K., Zamboni, N. & Sauer, U. Frontiers of high-throughput metabolomics. *Curr. Opin. Chem. Biol.* **36**, 15–23 (2017).

15. Miggiels, P., Wouters, B., van Westen, G. J. P., Dubbelman, A.-C. C. & Hankemeier, T. Novel technologies for metabolomics: More for less. *TrAC Trends Anal. Chem.* **120**, 115323 (2019).

16. Kohler, I., Hankemeier, T., van der Graaf, P. H., Knibbe, C. A. J. & van Hasselt, J. G. C. Integrating clinical metabolomics-based biomarker discovery and clinical pharmacology to enable precision medicine. *Eur. J. Pharm. Sci.* **109**, S15–S21 (2017).

17. Broeckhoven, K. & Desmet, G. The future of UHPLC: Towards higher pressure and/or smaller particles? *TrAC - Trends in Analytical Chemistry* vol. 63 65–75 (2014).

18. Kočová Vlčková, H. *et al.* Current state of bioanalytical chromatography in clinical analysis. *Analyst* **143**, 1305–1325 (2018).

19. Fekete, S., Schappler, J., Veuthey, J. L. & Guillarme, D. Current and future trends in UHPLC. *TrAC - Trends Anal. Chem.* **63**, 2–13 (2014).

20. Ruta, J., Rudaz, S., McCalley, D. V., Veuthey, J.-L. & Guillarme, D. A systematic investigation of the effect of sample diluent on peak shape in hydrophilic interaction liquid chromatography. *J. Chromatogr. A* **1217**, 8230–8240 (2010).

21. Desmet, G. & Eeltink, S. Fundamentals for LC Miniaturization. *Anal. Chem.* **85**, 543–556 (2013).

22. Hansen, F., Øiestad, E. L. & Pedersen-Bjergaard, S. Bioanalysis of pharmaceuticals using liquid-phase microextraction combined with liquid chromatography–mass spectrometry. *J. Pharm. Biomed. Anal.* **189**, (2020).

23. Ocaña-González, J. A., Fernández-Torres, R., Bello-López, M. Á. & Ramos-Payán, M. New developments in microextraction techniques in bioanalysis. A review. *Analytica Chimica Acta* vol. 905 8–23 (2016).

24. Friebel, A., von Harbou, E., Münnemann, K. & Hasse, H. Reaction Monitoring by Benchtop NMR Spectroscopy Using a Novel Stationary Flow Reactor Setup. *Ind. Eng. Chem. Res.* **58**, 18125–18133 (2019).

25. Lemos, V. A. *et al.* In-syringe dispersive liquid-liquid microextraction. *Talanta* **238**, (2022).

26. Gómez-Ríos, G. A. *et al.* Open Port Probe Sampling Interface for the Direct Coupling of Biocompatible Solid-Phase Microextraction to Atmospheric Pressure Ionization Mass Spectrometry. *Anal. Chem.* **89**, 3805–3809 (2017).

27. Alexovič, M., Horstkotte, B., Solich, P. & Sabo, J. Automation of static and dynamic non-dispersive liquid phase microextraction. Part 1: Approaches based on extractant drop-, plug-, film- and microflow-formation. *Anal. Chim. Acta* **906**, 22–40 (2016).

28. Alexovič, M., Horstkotte, B., Šrámková, I., Solich, P. & Sabo, J. Automation of dispersive liquid–liquid microextraction and related techniques. Approaches based on flow, batch, flow-batch and in-syringe modes. *TrAC - Trends Anal. Chem.* **86**, 39–55 (2017).

29. Miggiels, P., Wouters, B., van Westen, G. J. P., Dubbelman, A. C. & Hankemeier, T. Novel technologies for metabolomics: More for less. *TrAC - Trends in Analytical Chemistry* vol. 120 115323 (2019).

30. Drouin, N. *et al.* Electromembrane extraction of highly polar compounds: Analysis of cardiovascular biomarkers in plasma. *Metabolites* **10**, (2020).

31. He, Y. *et al.* A high-throughput, ultrafast, and online three-phase electro-extraction method for analysis of trace level pharmaceuticals. *Anal. Chim. Acta* **1149**, 338204 (2021).

32. Fuchs, D. *et al.* Direct coupling of a flow-flow electromembrane extraction probe to LC-MS. *Anal. Chim. Acta* **905**, 93–99 (2016).

33. Eibak, L. E. E., Rasmussen, K. E., Øiestad, E. L., Pedersen-Bjergaard, S. & Gjelstad, A. Parallel electromembrane extraction in the 96-well format. *Anal. Chim. Acta* **828**, 48–52 (2014).

34. Quist, J., Vulto, P. & Hankemeier, T. Isotachophoretic phenomena in electric field gradient focusing: perspectives for sample preparation and bioassays. *Anal. Chem.* **86**, 4078–87 (2014).

35. Fornells, E. *et al.* Evaporative membrane modulation for comprehensive two-dimensional liquid chromatography. *Anal. Chim. Acta* **1000**, 303–309 (2018).

36. Schoonen, J.-W. *et al.* Solvent Exchange Module for LC-NMR Hyphenation Using Machine Vision-Controlled Droplet Evaporation. *Anal. Chem.* **85**, 5734–5739 (2013).

37. Rivera, D. E., Morari, M. & Skogestad, S. Internal model control: PID controller design. *Ind. Eng. Chem. Process Des. Dev.* **25**, 252–265 (1986).

38. Bialkowski, W. L. Control of the Pulp and Paper Making Process. in *The Control Handbook* (ed. Levine, W. S.) 1219–1242 (CRC Press, 1996).

39. Ranz, W. E. & Marshall, W. R. Evaporation from drops: Part 1. *Chem. Eng. Prog.* **48**, 141–148 (1952).

40. Incropera, F. P., DeWitt, D. P., Bergman, T. L. & Lavine, A. S. *Introduction to Heat Transfer.* (John Wiley & Sons, 2007).

41. Hilpert, R. Wärmeabgabe von geheizten Drähten und Rohren im Luftstrom. *Forsch. auf dem Gebiete des Ingenieurwesens* **4**, 215–224 (1933).

42. Ganzevles, F. L. A. & Geld, C. W. M. va. der. Heat and mass transfer from internal flows to hemispheres and flat parts in between. *Int. J. Heat Mass Transf.* **41**, 3705–3718 (1998).

43. Fang, M. *et al.* Thermal Degradation of Small Molecules: A Global Metabolomic Investigation. *Anal. Chem.* **87**, 10935–10941 (2015).

44. Downing, C. G. The evaporation of drops of pure liquids at elevated temperatures: Rates of evaporation and wet-bulb temperatures. *AIChE J.* **12**, 760–766 (1966).

45. Renksizbulut, M. & Yuen, M. C. Experimental Study of Droplet Evaporation in a High-Temperature Air Stream. *J. Heat Transfer* **105**, 384–388 (1983).

46. Misyura, S. Y. Evaporation of a sessile water drop and a drop of aqueous salt solution. *Sci. Rep.* **7**, 14759 (2017).

47. Wang, Z., Orejon, D., Takata, Y. & Sefiane, K. Wetting and evaporation of multicomponent droplets. *Phys. Rep.* **960**, 1–37 (2022).

48. Gliński, J., Chavepeyer, G., Platten, J. K. & Smet, P. Surface properties of diluted aqueous solutions of normal short-chained alcohols. *J. Chem. Phys.* **109**, 5050–5053 (1998).

49. Cheong, W. J. & Carr, P. W. The Surface Tension of Mixtures of Methanol, Acetonitrile, Tetrahydrofuran, Isopropanol, Tertiary Butanol and Dimethyl-Sulfoxide with Water at 25°C. *J. Liq. Chromatogr.* **10**, 561–581 (1987).

50. Haynes, W. M. *CRC Handbook of Chemistry and Physics.* (CRC Press, 2017).

51. Samuelsson, J., Edström, L., Forssén, P. & Fornstedt, T. Injection profiles in liquid chromatography. I. A fundamental investigation. *J. Chromatogr. A* **1217**, 4306–4312 (2010).

52. Deridder, S., Desmet, G. & Broeckhoven, K. Numerical investigation of band spreading generated by flow-through needle and fixed loop sample injectors. *J. Chromatogr. A* **1552**, 29–42 (2018).

53. García-Alvarez-Coque, M. C., Baeza-Baeza, J. J. & Ramis-Ramos, G. Reversed Phase Liquid Chromatography. in *Analytical Separation Science, vol. 1* (eds. Anderson, J. L., Berthod, A., Pino Estévez, V. & Stalcup, A. M.) 159–198 (Wiley-VCH Verlag GmbH & Co. KGaA, 2015).

54. Nazario, C. E. D., Silva, M. R., Franco, M. S. & Lanças, F. M. Evolution in miniaturized column liquid chromatography instrumentation and applications: An overview. *J. Chromatogr. A* **1421**, 18–37 (2015).

55. Nazario, C. E. D., Fumes, B. H., Silva, M. R. da & Lanças, F. M. *Miniaturized column liquid chromatography. Nanomaterials in Chromatography: Current Trends in Chromatographic Research Technology and Techniques* (Elsevier Inc., 2018).

56. Vargas Medina, D. A., Maciel, E. V. S., de Toffoli, A. L. & Lanças, F. M. Miniaturization of liquid chromatography coupled to mass spectrometry. *TrAC Trends Anal. Chem.* **128**, 115910 (2020).

57. Dong, M. W. & Guillarme, D. UHPLC, part II: Benefits. *LC-GC North Am.* **35**, 486–495 (2017).

58. De Vos, J., Broeckhoven, K. & Eeltink, S. Advances in Ultrahigh-Pressure Liquid Chromatography Technology and System Design. *Anal. Chem.* **88**, 262–278 (2016).

59. Dolan, J. W. How Does It Work? Part 3: Autosamplers. *LCGC Eur.* **29**, 370–374 (2016).

60. Dolan, J. W. & Snyder, L. R. Injectors and Autosamplers. in *Troubleshooting LC Systems* 235–290 (Humana Press, 1989).

61. Anspach, J. A., Maloney, T. D., Brice, R. W. & Colón, L. A. Injection valve for ultrahigh-pressure liquid chromatography. *Anal. Chem.* **77**, 7489–7494 (2005).

62. Wren, S. A. C. & Tchelitcheff, P. Use of ultra-performance liquid chromatography in pharmaceutical development. *J. Chromatogr. A* **1119**, 140–146 (2006).

63. Vissers, J. P. C., De Ru, A. H., Ursem, M. & Chervet, J. P. Optimised injection techniques for micro and capillary liquid chromatography. *J. Chromatogr. A* **746**, 1–7 (1996).

Supplementary Information

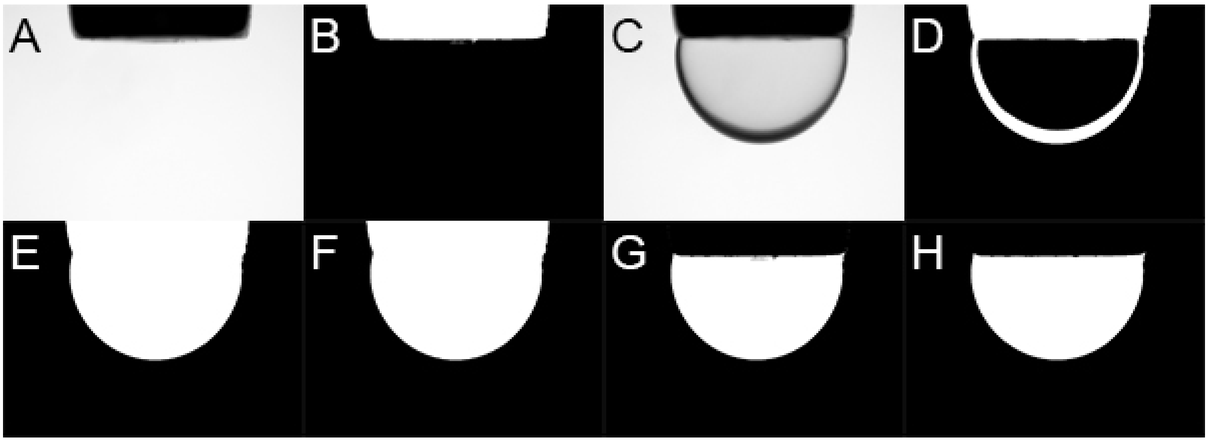

Figure S1. Image processing steps for the droplet volume calculation algorithm, in order: A) background image of the needle; B) binarized needle image; C) original droplet image; D) binarization with threshold; E) hole-filling; F) particle filter to remove unconnected pixels; G) needle subtraction; H) particle filter to remove unconnected pixels.

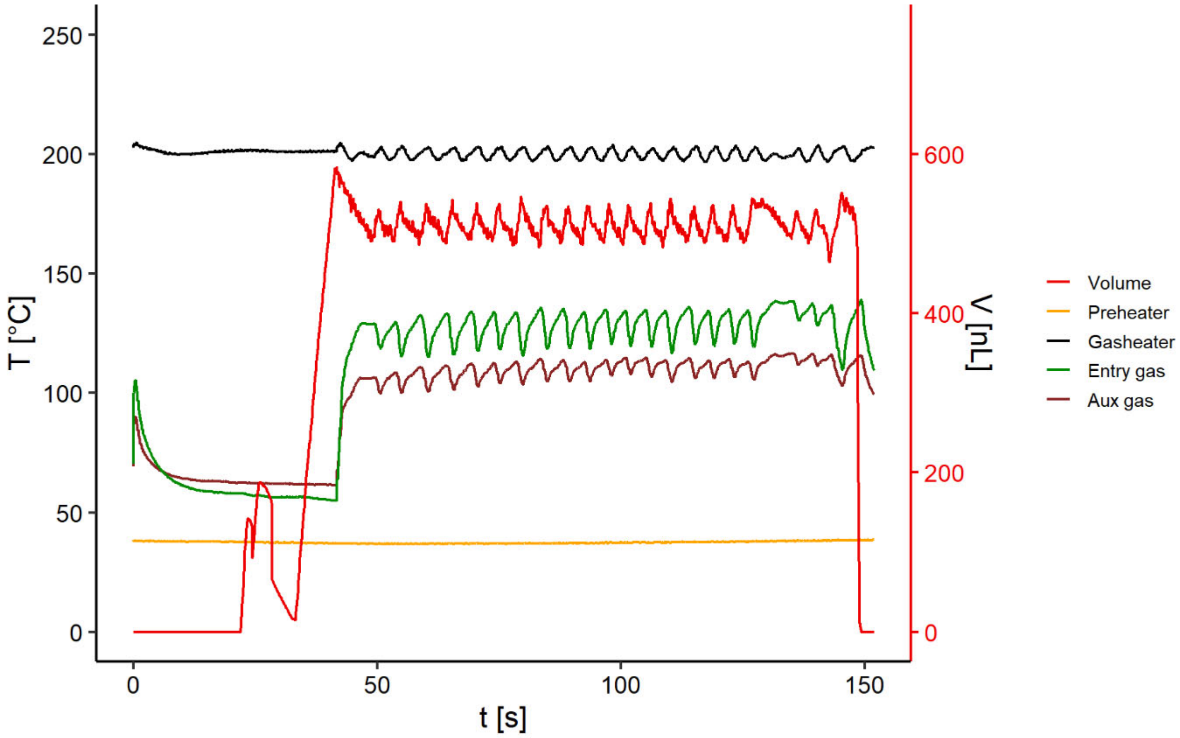

Figure S2. Droplet volume and (gas) temperatures recorded during the solvent evaporation from a 500 nL droplet of methylene blue in 50% MeOH at a rate of 6 µL/min.. The gas temperatures as well as the droplet volume show a mild oscillation as response to the fluctuating gas flow rate, regulated by the PI feedback control loop. The droplet volume remains stable within 50 nL of the setpoint value throughout the process.

Supplementary S3: Evaporation model

This model describes evaporation of a hemispherical droplet suspended from a stainless-steel needle in a free gas stream (Figure S2). An order-of-magnitude analysis showed that the heat transfer from the needle, acting as a fin in the free stream, cannot be neglected and it will therefore be taken into account. Without loss of generality, the droplet is considered a perfectly hemispherical cap with a base radius equal to the needle radius.

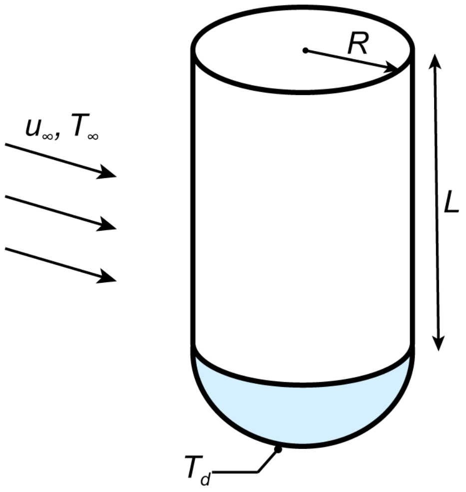

Figure S3. Hemispherical droplet suspended from a solid stainless steel needle, in a free stream of gas.

The model is obtained by setting up the coupled mass and energy balance for the system comprising both the droplet and the needle stem, seen as a fin of the droplet (Eq. 1). It states that the heat flux into the droplet is equal to the sum of the heat convected to the droplet, Q_{drop} (Eq. 2), and the heat convected to the fin, Q_{needle} (Eq. 3), minus the evaporation heat flux by mass transfer away from the droplet, $\dot{m}\Delta H_{vap}$. A pseudo-steady process condition is considered in which the temperature of the droplet does not change.

$$Q_{drop} + Q_{needle} - \dot{m}\Delta H_{vap} = 0 \tag{1}$$

$$Q_{drop} = h_d 2\pi R^2 (T_\infty - T_d) \tag{2}$$

$$Q_{needle} = h_n 2\pi R L (T_\infty - T_d)\eta_{fin} \tag{3}$$

$$\dot{m} = \pi R \mathbb{D} (c_s - c_\infty) Sh \tag{4}$$

This set of equations can be iteratively solved for the droplet temperature, T_d. In these equations the symbols are used: Q for heat flux, $\dot{m}$ for mass transfer, ΔH_{vap} for latent heat of vaporization, h for the average convective heat transfer coefficient, T for temperature, R the radius, L the needle length, η_{fin} the fin efficiency parameter, $\mathbb{D}$ the diffusion coefficient, c the vapor concentration, and Sh the Sherwood number. The subscripts denote: *d* for droplet, *n* for needle, *g* for gas, ∞ for free stream inflow conditions, and *s* saturation conditions. To solve this, firstly the dimensionless numbers Reynolds (Eq. 5), Sherwood (Eq. 6), and Schmidt (Eq. 7) are calculated, in which: ρ_g is the gas density, u_g is the average freestream velocity, D_n the needle diameter, and μ_g the gas dynamic viscosity.

$$Re_D = \frac{\rho_g u_g D_n}{\mu_g} \tag{5}$$

$$Sh = 2 + 0.6 \cdot Re^{\frac{1}{2}} \cdot Sc^{\frac{1}{3}} \tag{6}$$

$$Sc = \frac{\mu_g}{\rho_g \mathbb{D}} \tag{7}$$

With these dimensionless numbers, the conductive and convective heat transfer coefficients for the droplet are described by Eq. 8-11, with k_d the conductive heat transfer coefficient, h_d the convective heat transfer coefficient, Nu the Nusselt number, Pr the Prandtl number, $c_{p,g}$ the specific heat of the gas, and λ_g the thermal conductivity coefficient of the gas. The correlation for the Sherwood and Nusselt number of the droplet follows from Ranz & Marshall[1].

$$k_d = Sh \cdot \frac{\mathbb{D}}{2R} \tag{8}$$

$$h_d = Nu_d \cdot \frac{\lambda}{2R} \tag{9}$$

$$Nu_d = 2 + 0.6 Re^{\frac{1}{2}} Pr^{\frac{1}{3}} \tag{10}$$

$$Pr = \frac{c_{p,g} \mu_g}{\lambda_g} \tag{11}$$

The convective heat transfer coefficient of needle is given by Eq. 12-13 using the Hilpert correlation for a cylinder in crossflow[2]. The fin parameter and fin efficiency are given by Eq. 14 and 15, respectively, where the fin is assumed to be a finite cylinder in an infinite free stream. The thermal conductivity coefficient of the needle, λ_n, is considered to be a constant at the value of 13.4 W/m/K for stainless steel 316 at 300K[3].

$$h_n = Nu_n \cdot \frac{\lambda_g}{2R} \tag{12}$$

$$Nu_n = 0.683 \cdot Re^{0.466} Pr^{\frac{1}{3}} \tag{13}$$

$$m = \sqrt{\frac{2h_n}{\lambda_n R}} \tag{14}$$

$$\eta_{fin} = \frac{\tanh(mL)}{mL} \tag{15}$$

The empirical correlations used hold for a film model. As such the physical properties in the boundary layer are evaluated at the film temperature, T_f, the mean of the free stream and the droplet surface temperature (Eq. 16). The subscript f from here on denotes film conditions. The gas density and velocity at the film temperature can be calculated from the free stream conditions using the ideal gas law for an isobaric expansion (Eq. 17-18). It is assumed that the gas leaves the mass flow controller at a temperature of 293 K, before being heated to the freestream temperature. The gas velocity after the mass flow controller is calculated according to Eq. 19 with $\dot{q}$ the volumetric gas flow rate and A cross-sectional area of $23.678 \cdot 10^{-6}$ m. The nitrogen gas properties $c_{p,g}$, λ_g and μ_g, the latent heat of evaporation for water, ΔH_{vap}, and the diffusion coefficient of water in nitrogen, $\mathbb{D}$, are estimated by interpolating from the values in Table S1.

$$T_f = \frac{T_d + T_\infty}{2} \tag{16}$$

$$\rho_g = \rho_{T_{ref}} \frac{T}{T_{ref}} = 1.16 \frac{T_\infty}{293} \tag{17}$$

$$u_g = u_0 \frac{T_f}{T_{ref}} = u_0 \frac{T_f}{293} \tag{18}$$

$$u_0 = \frac{\dot{q}}{A} \tag{19}$$

The vapor saturation properties are evaluated at the droplet temperature, T_d. The saturation pressure is calculated using the Antoine equation[5] and converted from mmHg to Pa with the factor $\frac{10^5}{650}$ (Eq. 20). The saturation concentration is calculated from this using the Ideal Gas Law with the molecular weight for nitrogen, $M_w = 0.018$ kg/mol, and the universal gas constant $R_g = 8.314$ J/mol/K (Eq. 21). It is assumed that the heated inflowing gas is dry, $c_\infty = 0$.

$$P_{sat} = 10^{A - \frac{B}{C+T}} = 10^{8.07131 - \frac{1730.63}{233.426 + T_d - 273.15}} \cdot \frac{10^5}{650} \tag{20}$$

$$c_{sat} = P_{sat,T} \frac{M_w}{R_g T_d} \tag{21}$$

Table S1. Physical properties for nitrogen gas and water at various temperatures and p=1.0 bar.

$\mathbf{T}$ (K)	$c_{p,g}$ (J/kg/K)[a]	$\lambda_g \cdot 10^3$ (W/m/K)[a]	$\mu_g \cdot 10^7$ (Pa.s)[a]	$\mathbf{T}$ (K)	ΔH_{vap} (kJ/kg)[a]	$\mathbf{T}$ (K)	$\mathbb{D} \cdot 10^5$ (m²/s)[b]
250	1042	22.2	154.9	273.15	2502	282	2.21
300	1041	25.9	178.2	275	2497	298	2.53
350	1042	29.3	200.0	295	2449	327.5	3.05
400	1045	32.7	220.4	305	2426	353	3.60
450	1050	35.8	239.6	315	2402	373	3.96
				325	2378		
				335	2354		
				345	2329		
				355	2304		
				365	2278		
				373.15	2257		
				375	2252		

[a] Incropera & DeWitt, Introduction to Heat Transfer, 5th edition[3]

[b] O'Connell et al. 1969[4]

References

1. Ranz, W. E. & Marshall, W. R. Evaporation from drops: Part 1. *Chem. Eng. Prog.* **48**, 141–148 (1952).
2. Hilpert, R. Wärmeabgabe von geheizten Drähten und Rohren im Luftstrom. *Forsch. auf dem Gebiete des Ingenieurwesens* **4**, 215–224 (1933).
3. Incropera, F. P., DeWitt, D. P., Bergman, T. L. & Lavine, A. S. *Introduction to Heat Transfer.* (John Wiley & Sons, 2007).
4. O'Connell, J. P., Gillespie, M. D., Krostek, W. D. & Prausnitz, J. M. Diffusivities of water in nonpolar gases. *J. Phys. Chem.* **73**, 2000–2004 (1969).

5. Antoine, C. Tensions des vapeurs; nouvelle relation entre les tensions et les températures. *Comptes Rendus des Séances l'Académie des Sci.* **107**, (1888).

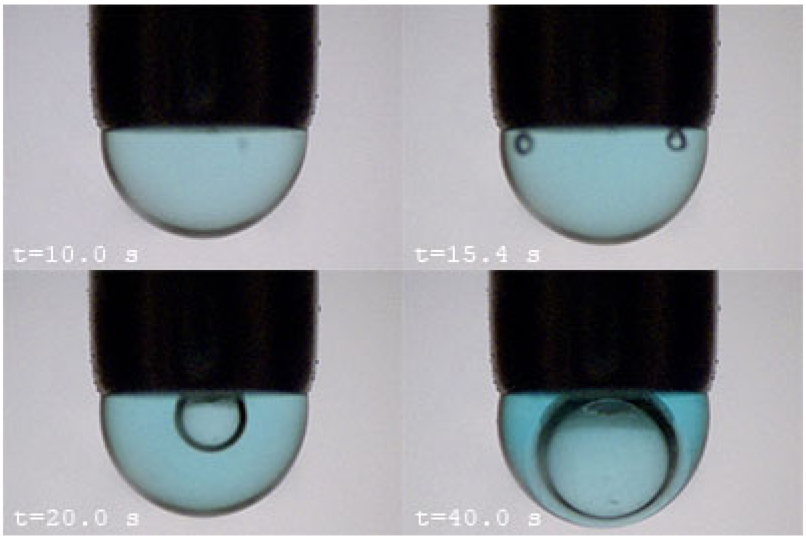

Figure S4. Formation of a vapor bubbles inside the evaporating droplet. Stills from the preconcentration of 8.0 to 0.8 μL of 5.0 μg/mL methylene blue in 30:70 water:acetonitrile, with a gas inflow temperature of 150-165 °C and an evaporation rate of 6 μL/min.